

X-RAY HOTSPOTS IN THE NORTHWEST SHELL OF THE SUPERNOVA REMNANT RX J1713.7–3946

RYOTA HIGURASHI,¹ NAOMI TSUJI,² AND YASUNOBU UCHIYAMA¹

¹*Department of Physics, Rikkyo University, 3-34-1 Nishi Ikebukuro, Toshima-ku, Tokyo 171-8501, Japan*

²*Interdisciplinary Theoretical & Mathematical Science Program (iTHEMS), RIKEN, 2-1 Hirosawa, Saitama 351-0198, Japan*

(Received MM DD, YYYY; Revised MM DD, YYYY; Accepted MM DD, YYYY)

ABSTRACT

The supernova remnant (SNR) RX J1713.7–3946 is one of the best-studied accelerators of cosmic rays because of its strong nonthermal X-ray and gamma-ray radiation. We have analyzed accumulated *Chandra* observations with a total exposure time of ~ 266 ks in the northwest rim of RX J1713.7–3946. We detect a substantially large number of point-like sources, referred to as “hotspots”, which are likely associated with the remnant. The spectra of the hotspots are well described by an absorbed power-law model. The spectral properties ($10^{21} \text{ cm}^{-2} \lesssim N_H \lesssim 10^{23} \text{ cm}^{-2}$ and $0.5 \lesssim \Gamma \lesssim 6$) are different from diffuse X-ray emission in RX J1713.7–3946, and the harder hotspot tends to have the larger N_H . We also confirm yearly and monthly variabilities of flux for some hotspots. We propose that RX J1713.7–3946 is embedded in a complex surroundings where some dense molecular clumps and cores exist inside a wind-blown cavity, and that the hotspot traces synchrotron emission caused by an interaction of shock waves of the SNR and dense molecular cores with a number density of $10^5 - 10^7 \text{ cm}^{-3}$. The X-ray radiation of the hotspot might be emitted from both primary electrons accelerated at the shocks and secondary electrons produced by the interaction of accelerated protons with the cores.

Keywords: acceleration of particles — ISM: individual objects (RX J1713.7–3946) — ISM: supernova remnants — radiation mechanisms: non-thermal — X-rays: ISM

1. INTRODUCTION

Supernova remnants are considered as the primary accelerators of the Galactic cosmic ray with energies smaller than the “knee” (a few PeV). The well-studied theory of diffusive shock acceleration (DSA) (Axford et al. 1977; Krymskii 1977; Bell 1978; Blandford & Ostriker 1978) is widely accepted for acceleration at shock waves of the supernova remnant (SNR). Koyama et al. (1995) first discovered synchrotron X-ray emission in the energy range of 0.4–8.0 keV radiated from electrons accelerated up to multi-TeV energies in the shell of SN 1006. The subsequent detection of synchrotron X-rays from other SNRs, including RX J1713.7–3946 (Koyama et al. 1997), makes SNRs among the best candidates for studying particle acceleration. Gamma-ray emission from SNRs that include RX J1713.7–3946 is also detected in the range of GeV–TeV energy (e.g., Funk (2015) and references therein), and this supports particle acceleration in SNRs. Accelerated protons pro-

duce gamma rays via decay of neutral pions produced by collisions with ambient protons or nuclei (“hadronic scenario”). Accelerated electrons might also generate gamma rays by inverse Compton (IC) scattering of low-energy photons (“leptonic scenario”). Gamma-ray radiation from accelerated protons was revealed by the detection of so-called “pion bumps” in middle-aged SNRs interacting with molecular clouds (Ackermann et al. 2013; Jogler & Funk 2016), whereas no obvious evidence has yet been found that protons are accelerated to the knee in SNRs.

The shell-type SNR RX J1713.7–3946 (also known as G347.3–0.5) was first discovered by *ROSAT* All-Sky Survey (Pfeffermann & Aschenbach 1996). The distance was estimated to be ~ 1 kpc by tracing the CO lines from the associated molecular clouds (Fukui et al. 2003). Its association with one of the historical SNRs, namely SN393, has been discussed (Wang et al. 1997; Fesen et al. 2012). Recent measurements of the forward shock velocity suggested the SN–SNR association, supporting an SNR age of ~ 1600 yr (Tsuji & Uchiyama 2016; Acero et al. 2017a). RX J1713.7–3946 is one

of the best-studied objects for investigating particle acceleration because of its strong non-thermal X-ray and gamma-ray emissions.

The X-ray emission of RX J1713.7–3946 is dominated by non-thermal radiation, i.e., synchrotron radiation that is emitted by very-high-energy electrons accelerated in the SNR shock via DSA (Koyama et al. 1997; Slane et al. 1999; Uchiyama et al. 2003; Cassam-Chenaï et al. 2004; Hiraga et al. 2005; Takahashi et al. 2008; Tanaka et al. 2008). The acceleration efficiency was found to be close to the maximum rate (Bohm limit) based on the X-ray observations (Uchiyama et al. 2007; Tanaka et al. 2008; Tsuji et al. 2019). Katsuda et al. (2015) detected thermal X-ray components in the inner region. They inferred that the thermal line emission originates from the ejecta heated by the reverse shock, and the mass of the progenitor is estimated to be $\lesssim 20 M_{\odot}$ by the composition of its ejecta. In the shell region, complex filamentary structures have been revealed by *Chandra* with its superb angular resolution ($0.5''$) (Uchiyama et al. 2003; Lazendic et al. 2004). Okuno et al. (2018) lately presented the spatially resolved spectroscopy of the SNR with *Chandra*. They showed that the filamentary structures in the southeast (SE) have harder spectra ($\Gamma \sim 2.0$) than the surrounding regions, whereas those in the southwest (SW) have relatively soft spectra ($\Gamma \sim 2.7$) because of the deceleration of shock waves which are interacting with the clumpy interstellar medium produced by the stellar wind of the massive progenitor star. Recently, *NuSTAR* observations of the northwest (NW) rim obtained a spatially resolved X-ray image in the 10–20 keV energy band (Tsuji et al. 2019). The hard X-ray morphology is roughly in agreement with the soft-band images of previous works.

RX J1713.7–3946 is known as a strong TeV gamma-ray emitter (Aharonian et al. 2006, 2007), but the radiation mechanism (“hadronic” and/or “leptonic”) has been in a matter of debate (e.g., Uchiyama et al. 2003; Aharonian et al. 2006; Tanaka et al. 2008; Ellison et al. 2010; Zirakashvili & Aharonian 2010; Abdo et al. 2011; Fukui et al. 2012; Inoue et al. 2012; Sano et al. 2013; Gabici & Aharonian 2014; Celli et al. 2019; H.E.S.S. Collaboration et al. 2018). The spatial coincidence between the non-thermal X-ray and the TeV gamma ray may imply that the parent particles responsible for these two radiations are identical, i.e., electrons. The leptonic radiation also seems to be favored by a hard spectrum in the GeV energy band observed with *Fermi*-LAT (Abdo et al. 2011). The observed photon index ($\Gamma = 1.5 \pm 0.1$) in the bandpass of *Fermi*-LAT is reconciled with the IC gamma ray radiated from the electron population with a spectral index of 2, which is expected from stan-

dard acceleration via DSA. Note that a simple modeling with unique population of electrons fails to reproduce the multi-wavelength spectrum (H.E.S.S. Collaboration et al. 2018). It has lately been shown that the observed GeV–TeV gamma-ray spectrum can be reproduced by the hadronic scenario as well (Inoue et al. 2012; Gabici & Aharonian 2014; Celli et al. 2019). Because RX J1713.7–3946 is located in a complex region in the Galactic Plane, there exist target materials to produce π^0 -decay gamma rays through the pp interaction (see below for details). Although deeper H.E.S.S. observations with total live time of 164 h have been conducted, the mechanism of the gamma-ray radiation remains ambiguous (H.E.S.S. Collaboration et al. 2018). There are several ways to distinguish the gamma-ray origin, such as by detection of synchrotron emission from a secondary electron produced by the decay of a charged pion in the pp interaction (Huang et al. 2018) or by accurate observation around 100 TeV with Cherenkov Telescope Array (CTA) because the Klein–Nishina effect would suppress the leptonic emission component (Acero et al. 2017b). The confirmation of the hadronic component would also come from observations of neutrinos, with large volume instruments as KM3NeT (Ambrogio et al. 2018).

RX J1713.7–3946 is located in the complex environment of ambient molecular clouds (Fukui et al. 2003, 2012). The progenitor star is expected to have exploded in a cavity wall produced by the stellar wind from the massive progenitor star. In this case, dense materials, such as molecular clumps and molecular cores, could have survived against the wind. Here, we refer to a “clump” as a denser part inside a molecular cloud with a number density of $10^3 - 10^4 \text{ cm}^{-3}$ and a typical size of 0.1 pc, and a “core” as a much denser part inside the clump with a number density of $10^5 - 10^7 \text{ cm}^{-3}$ and a typical size of 0.01 pc. The medium with a lower density is thought to be swept up before the SN explosion. This results in the complex surrounding which has some molecular clumps and cores inside the wind-blown cavity, as mentioned in Slane et al. (1999); Inoue et al. (2012); Katsuda et al. (2015).

Shock–cloud interactions in such complex circumstances have been studied with magnetohydrodynamical simulations. Inoue et al. (2012) revealed that the magnetic field is amplified up to 1 mG in a small region (~ 0.05 pc), resulting from the SNR shock propagating within the clumpy environment. Recently, Celli et al. (2019) showed that magnetic field amplification occurs at a thin region (referred to as “skin”) with a size of ~ 0.05 pc at the surface of the molecular clump.

Observations have been in agreement with the picture of the shock–cloud interaction in RX J1713.7–

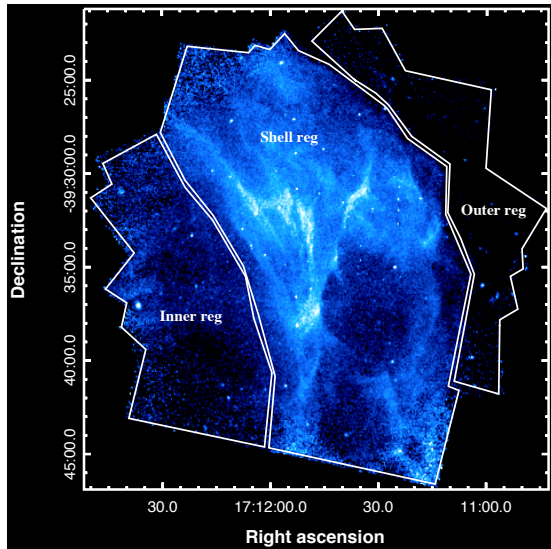


Figure 1. The combined flux image of RX J1713.7–3946 NW at 0.5 – 7.0 keV. Each pixel has a width of 1 arcsec. The three white regions indicate “Inner reg”, “Shell reg”, and “Outer reg”.

–3946 (Fukui et al. 2003, 2012; Moriguchi et al. 2005; Sano et al. 2010, 2013). Using observations with *Suzaku*, Sano et al. (2015) reported a parsec-scale correlation between the intensities of the non-thermal X-ray emission and the molecular clumps. They also found an anti-correlation between the X-ray radiation and the molecular clumps on a sub-parsec scale. This suggested that the synchrotron X-ray intensity is indeed strong in the surroundings of the clumps where the magnetic field is expected to be enhanced. Okuno et al. (2018) showed a similar anti-correlation between molecular clumps and the photon indices of the X-ray spectra with *Chandra*. The presence of a magnetic field with $B \sim 1$ mG was reported in small knot-like regions in the NW shell of RX J1713.7–3946, inferred from the detection of year-scale variability caused by a balance between the synchrotron emission and the acceleration (Uchiyama et al. 2007).

Here, we report the detection of a significantly larger population of point-like sources in the NW rim of RX J1713.7–3946. In Section 2, we summarize the *Chandra* observations. Detailed analyses and results are presented in Section 3. We discuss the physical meaning of the newly found sources in Section 4. The conclusions are given in Section 5.

2. OBSERVATIONS AND DATA REDUCTION

We performed observations of RX J1713.7–3946 NW with the *Chandra* Advanced CCD Imaging Spectrometer (ACIS)-I six times from 2005 to 2011 (Table 1). We also made use of archival data taken in 2000. The total exposure time reached ~ 266 ks, which allowed us

to investigate relatively faint structures. Moreover, the seven-time observations over a span of eleven years, from 2000 to 2011, enabled us to explore both year-scale and month-scale variability by utilizing the three observations taken in 2009. Taking advantage of the great angular (sub-arcsecond) resolution of *Chandra* and the accumulated rich statistics, we performed a detailed analysis of small and characteristic structures in the NW rim of RX J1713.7–3946. All the data were reprocessed using `chandra_repro` with CALDB version 4.7.6 in Chandra Interactive Analysis of Observations (CIAO) version 4.9, provided by the Chandra X-Ray Center (CXC).

3. ANALYSIS AND RESULTS

3.1. Hotspot

We present a flux image at 0.5–7.0 keV of the NW shell of RX J1713.7–3946 in Figure 1. This image was generated using `merge_obs` in CIAO, which combined all the observations of RX J1713.7–3946 listed in Table 1. We found many bright, point-like sources, and conducted a detailed study to investigate the properties of these point-like structures.

We selected 65 sources in the following procedure and defined them as “hotspots. First, the point-like sources were systematically picked up using `wavdetect` in CIAO. In this process, we used a combined count map in the range of 0.5–7.0 keV and a combined point spread function (PSF) map that is weighted by an exposure time of each epoch. We ran `wavdetect` with the “wavelet scale of 1 and 2, which is a parameter of a radius of the wavelet function (see Freeman et al. (2002) for details). This resulted in the detection of 154 sources. Second, we set a criterion of the photon flux to be larger than 1.0×10^{-6} photon $\text{cm}^{-2} \text{s}^{-1}$, reducing the number of the detected sources to 65. The detection significance of these 65 sources was more than 4σ . Note that sources with photon fluxes smaller than the criterion value have limited statistics, causing large uncertainty in the spectral analysis. In this study, we analyzed in detail the properties of the 65 hotspots, hereafter labeled as HS01 to HS65. We show their locations in the NW rim of the SNR in Figure 2. HS01 to HS65 are labeled in the order of their X-ray brightness. Their locations and the other properties (obtained below) are summarized in Table 3.

Most of the hotspots were spatially consistent with the point-like sources, whereas some showed slight spatial extension. We could not confidently test their spatial extension due to the poor statistics.

We confirmed that the NW shell of RX J1713.7–3946 contains many hotspot-like structures. Figure 3 illustrates the surface density of the hotspot, i.e., summing the number of hotspots contained in “Shell reg”, “In-

Table 1. *Chandra* observations of RX J1713.7–3946 NW, CTB 37A and IC 4637

ObsID	Target name	Start date (yyyy-mm-dd)	Pointing position		Exposure (ks)	A.D. [†] (arcmin)
			(α [J2000], δ [J2000])	(l , b) [*]		
736	RX J1713.7–3946 NW	2000-07-25	17:11:49.9, −39:36:14.7	347.2660, −0.1121	29.6	–
5560	RX J1713.7–3946 NW	2005-07-09	17:11:45.5, −39:33:40.0	347.2923, −0.0752	29.0	–
6370	RX J1713.7–3946 NW	2006-05-03	17:11:46.3, −39:33:12.0	347.3001, −0.0728	29.8	–
10090	RX J1713.7–3946 NW	2009-01-30	17:11:44.4, −39:32:57.1	347.2999, −0.0654	28.4	–
10091	RX J1713.7–3946 NW	2009-05-16	17:11:46.3, −39:32:55.7	347.3038, −0.0701	29.6	–
10092	RX J1713.7–3946 NW	2009-09-10	17:11:46.1, −39:33:51.6	347.3043, −0.0689	29.2	–
12671	RX J1713.7–3946 NW	2011-07-01	17:11:47.5, −39:33:41.2	347.2959, −0.0807	89.9	–
6721	CTB 37A	2006-10-07	17:14:35.8, −38:31:24.6	348.4558, +0.0879	19.9	70.3
14586	IC 4637	2014-03-07	17:05:10.5, −40:53:08.4	345.4794, +0.1403	29.6	109.8

^{*}Galactic longitude and latitude coordinates expressed in degrees.

[†]Angular distance from RX J1713.7–3946 NW with ObsID of 12671.

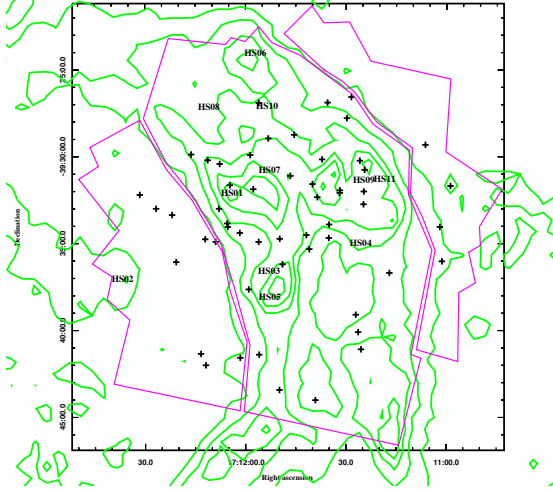


Figure 2. The locations of HS01–HS65 in the NW rim of RX J1713.7–3946. HS01 to HS11 (top 11 brightest hotspots) are shown with their names, whereas the others are shown with black crosses. The contour is taken with *XMM-Newton* (0.5–8 keV), and the magenta regions are the same regions shown in Figure 1.

ner reg, and “Outer reg, shown in Figure 1, divided by their areas. The radial widths of these regions are roughly $\sim 0.2^\circ$ (Shell reg), $\sim 0.1^\circ$ (Inner reg), and $\sim 0.1^\circ$ (Outer reg), assuming the center of the SNR being ($17^{\text{h}}13^{\text{m}}25.2^{\text{s}}$, $-39^{\text{d}}46^{\text{m}}15.6^{\text{s}}$) (H.E.S.S. Collaboration et al. 2018). The azimuthal angle of these regions from the center is $\sim 60^\circ$. There is clearly an excess number of hotspots in the shell, which is one of the brightest regions in the whole SNR. Because the NW part of RX J1713.7–3946 is located in the Galactic Plane, many X-ray sources likely exist both in the

foreground and background. However, we found that the number of the hotspot is quite large in RX J1713.7–3946 NW, as follows. We applied the same method of detecting hotspot-like features to the other two *Chandra* observations performed in the vicinity of RX J1713.7–3946, namely, SNR CTB 37A and the planetary nebula IC 4637. They are $70.3'$ and $109.8'$ away from the NW rim of RX J1713.7–3946, respectively (Table 1). Note that we extracted the source-free region for the observation of CTB 37A. The surface density of the hotspots from these two observations are also shown in Figure 3, labeled as “CTB 37A” and “IC 4637”. The larger population of hotspots in the NW shell of RX J1713.7–3946 suggests that the hotspots could be associated with the remnant.

We estimated the number of hotspots in the shell of the SNR. The average of the surface density obtained from CTB 37A and IC 4637 was $\sim 0.049 \text{ arcmin}^{-2}$, and used as background. Then, the net surface density calculated from the two regions of “Shell reg” and “Inner reg” was estimated to be $0.167 \text{ arcmin}^{-2}$. If we assume the surface density is uniform in the entire shell, simply describes by an annulus with the inner and outer radii of 0.2° and 0.5° , respectively, the number of hotspots in the entire shell of the SNR is estimated as ~ 400 .

3.2. Flux Image

We produced flux images in three energy bands, 0.5–1.2 keV (soft), 1.2–2.0 keV (medium), and 2.0–7.0 keV (hard). All seven epochs were combined with `merge_obs`, setting the bin size to 2 (i.e., one pixel corresponds to $1''$). The flux images of the three example hotspots (HS01, HS04, and HS05) are shown in Figure 4.

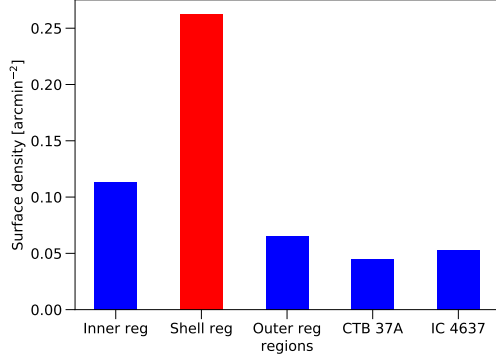


Figure 3. The surface density of hotspot in RX J1713.7–3946 NW, CTB 37A, and IC 4637. We divide the NW region of RX J1713.7–3946 into three regions, labeled Inner reg, Shell reg, and Outer reg, as shown in Figure 1.

As shown in the figure, there are various types of hotspots seen differently in the different energy channels: HS01 is bright in the soft band, whereas HS05 is dark in the soft and medium bands. This suggests that their spectra would also vary depending on the hotspots, which is presented in the next subsection.

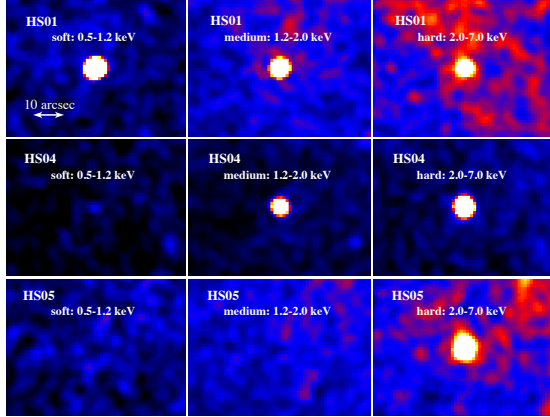


Figure 4. Flux images of the three hotspots (HS01, HS04, and HS05 from the top), shown in the three energy bands of 0.5 – 1.2 keV, 1.2 – 2.0 keV, and 2.0 – 7.0 keV from the left.

3.3. Spectrum

We performed spectral analysis of the hotspot. The spectrum of each hotspot was extracted from a circular region with a radius of $5''$ using `specextract` in CIAO. We then subtracted the background, which was extracted from an annulus region with the inner and outer radii of $8''$ and $27''$, respectively. Both the source and background regions had the same central coordinate, which was detected by `wavdetect` in Section 3.1. In the following spectral analysis, we used XSPEC ver-

sion 12.9.1 included in HEASoft version 6.21. The uncertainties in this paper indicate 1σ .

We used an absorbed (TBabs in XSPEC; [Wilms et al. \(2000\)](#)) power-law model to fit the spectra. We jointly fitted the spectra of the different epochs: we tied the parameters of the model (a photon index Γ and a column density of interstellar absorption N_H) with the all spectra and set the normalization free for each epoch. Figure 5 presents the spectra of the three hotspots (HS01, HS04, and HS05), shown with the best-fit model. In Table 3, the results of each hotspot are summarized. The upper and lower limits were set at a 1σ confidence level. The flux in the energy band of 0.5–7.0 keV was calculated for each observation, and the minimum and maximum values are shown in Table 3. Furthermore, because hotspots are dark at certain epochs, spectral fit could not be well performed using all the observation data. In this case, the fitting was performed using only epochs in which the hotspot was bright enough, thus only the maximum value of the energy flux is shown in Table 3. It should be noted that some hotspots with poor statistics were not well-fitted, and their results are shown as “–” in Table 3.

In Figure 6, we show the N_H – Γ diagram, derived from the spectral fitting of each hotspot. Note that bright hotspots (HS01–HS11) are highlighted with red thick lines. Figure 6 does not include the results of hotspots whose spectral parameters were not well constrained and were obtained only with the upper and lower limits. The typical values of N_H of $(0.7 - 1.0) \times 10^{22} \text{ cm}^{-2}$ and Γ of 2.3–2.6 in RX J1713.7–3946 NW are shown with the cyan region. As shown in Figure 6, the spectral features of the hotspots substantially deviate from the typical values. There is an anti correlation between N_H and Γ : the N_H of hotspot is larger for the smaller Γ . It should be noted that we subtracted the spectral component of the SNR as the background. Therefore, the spectrum of the hotspot has a pure X-ray emission from itself, and it does not contain any emission from the remnant. We emphasize that the spectrum of the hotspot indicates a significantly different spectrum expected for the non-thermal (synchrotron) radiation in RX J1713.7–3946. The origin of these spectra is discussed in Section 4.

We also fitted the spectra of HS01, HS04, and HS05 with thermal models, Bremsstrahlung and black-body radiation. The column density was fixed to the best-fit value derived from using the power-law model. The results are presented in Table 2. The power-law model is favored inferred from the chi-squared value, although the limited statistics do not confidently exclude the thermal origin. However, the featureless spectrum and the relatively higher temperature obtained for the thermal

Table 2. The best-fit parameters of HS01, HS04, and HS05

HS	Model*	N_H (10^{22} cm^{-2})	$\Gamma/k_B T$ (/keV)	Flux [†] (min) ($10^{-14} \text{ erg cm}^{-2} \text{ s}^{-1}$)	Flux [†] (max) ($10^{-14} \text{ erg cm}^{-2} \text{ s}^{-1}$)	χ^2/dof
HS01	PL	$0.423^{+0.095}_{-0.084}$	$4.22^{+0.35}_{-0.30}$	$2.47^{+0.45}_{-0.91}$	$7.19^{+0.98}_{-0.94}$	315.1/289
HS01	Bremss	0.423 (fix)	$0.386^{+0.020}_{-0.019}$	$2.25^{+0.58}_{-0.47}$	$5.97^{+0.70}_{-0.63}$	344.8/290
HS01	Bbody	0.423 (fix)	$0.176^{+0.005}_{-0.005}$	$2.11^{+0.52}_{-0.38}$	$5.41^{+0.61}_{-0.68}$	370.1/290
HS04	PL	$4.42^{+0.49}_{-0.45}$	$3.37^{+0.26}_{-0.24}$	$4.22^{+0.33}_{-1.01}$	$6.90^{+0.31}_{-1.10}$	188.8/186
HS04	Bremss	4.42 (fix)	$1.41^{+0.10}_{-0.09}$	$3.92^{+0.54}_{-0.67}$	$6.40^{+0.58}_{-0.63}$	200.1/187
HS04	Bbody	4.42 (fix)	$0.51^{+0.02}_{-0.02}$	$3.50^{+0.46}_{-0.51}$	$5.60^{+0.61}_{-0.50}$	239.4/187
HS05	PL	$19.72^{+7.62}_{-5.94}$	$1.02^{+0.78}_{-0.67}$	$3.62^{+0.24}_{-1.43}$	$23.45^{+0.41}_{-7.85}$	145.2/172
HS05	Bremss [‡]	19.72 (fix)	—	—	—	—
HS05	Bbody	19.72 (fix)	$1.65^{+0.19}_{-0.15}$	$3.42^{+0.43}_{-0.64}$	$22.91^{+0.96}_{-2.41}$	145.74/173

*PL, Bremss, and Bbody represent the models of the power law, Bremsstrahlung, and black body, respectively.

[†]Flux is calculated in the range of 0.5 – 7.0 keV

[‡]The spectrum of HS05 is not able to fit with the Bremsstrahlung model.

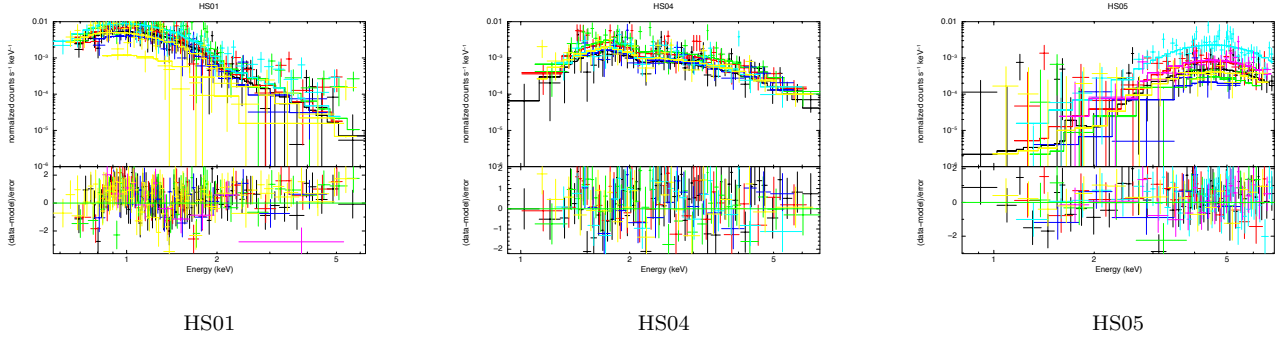


Figure 5. The spectrum of HS01, HS04, and HS05 from the left panel, shown with the absorbed power-law model. The different colors represent the different epochs: the black spectrum was taken in 2011, red in September 2009, green in May 2009, blue in January 2009, cyan in 2006, magenta in 2005, and yellow in 2000.

model might support non-thermal radiation, namely, the synchrotron emission from the accelerated electrons (see Section 4 for details).

3.4. Time Variation

In this section, we discuss the time variation of the hotspots. Figure 7 presents light curves of the three hotspots, where the brightness was calculated by summing up the flux values inside a circular region with a radius of $5''$. The three hotspots show varying brightness from time to time. We evaluated the time variability using a chi-squared (χ^2) test. The chi-squared value is given by

$$\chi^2 = \sum_i \frac{(f_i - f_c)^2}{\sigma_i^2}, \quad (1)$$

where i , f_i , f_c , and σ_i are a subscript notating each observation, the brightness, the constant value, and the error of the brightness, respectively. Once the minimum χ^2 value (χ_{\min}^2) is found by changing f_c , we derived the confidence to exclude the hypothesis of no time variation from the value of χ_{\min}^2 . The constant value that gives χ_{\min}^2 is also shown in Figure 7.

We found that 20 hotspots showed time variations at more than 3σ confidence level, and 34 hotspots do so at more than 2σ (see Table 3). We note that 8 hotspots varied not only on a year-scale but also on a month-scale with more than 3σ , inferred from the same chi-squared test using the three data taken in 2009. The observed time variation may contain an important key for interpreting the origin of the hotspots: in fact a short

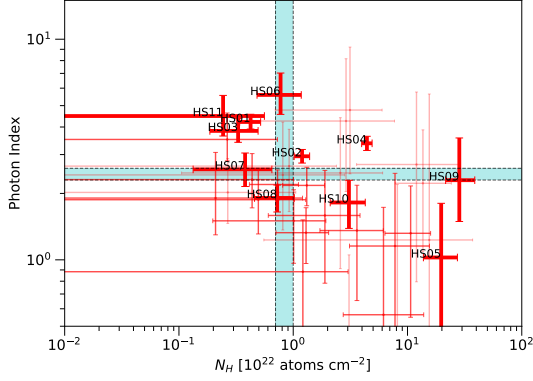


Figure 6. Diagram of the column density (N_H) and the photon index (Γ) derived from the spectral fitting of each hotspot with the absorbed power-law model. Typical N_H of $(0.7 - 1.0) \times 10^{22} \text{ cm}^{-2}$ and Γ of $2.3 - 2.6$ in the NW shell of RX J1713.7–3946 are shown in the cyan region. Note that the results of the bright hotspot are highlighted with the thick red lines.

time variation indicates a strong magnetic field of $\sim \text{mG}$ intensity, as discussed in Uchiyama et al. (2007).

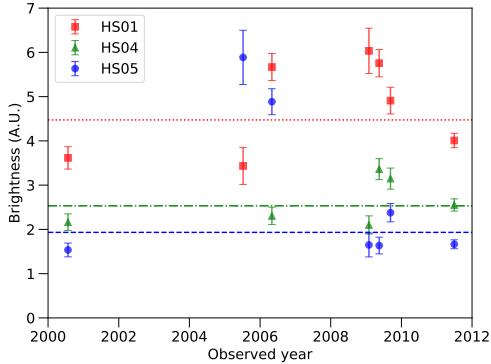


Figure 7. Light curves of HS01 (shown with red squares), HS04 (green triangles), and HS05 (blue circles). The horizontal lines represent the constant values that give χ^2_{\min} in chi-squared test (see also the text).

4. DISCUSSION

Our observations revealed the significantly large population of hotspots in RX J1713.7–3946 NW, the trend of the spectra (the larger N_H , the smaller Γ), and the yearly and monthly variabilities of the flux. We suggest that the hotspots are attributed to synchrotron radiation resulting in the interaction between a dense molecular core and the SNR shock. An inhomogeneous environment, where the dense core and clumps have survived against the stellar wind from the massive progenitor star, is possible for SNR RX J1713.7–3946. When the

SNR shock interacts with the cores, synchrotron emission is expected due to an enhanced magnetic field surrounding the core (Inoue et al. 2012; Celli et al. 2019).

The timescales of synchrotron cooling and acceleration of electrons of energy E_e are respectively given by

$$t_{\text{synch}} \approx 12 \left(\frac{B}{\text{mG}} \right)^{-2} \left(\frac{E_e}{\text{TeV}} \right)^{-1} \text{ yr},$$

$$\approx 1.5 \left(\frac{B}{\text{mG}} \right)^{-3/2} \left(\frac{\varepsilon}{\text{keV}} \right)^{-1/2} \text{ yr}, \quad (2)$$

and

$$t_{\text{acc}} \approx 1\eta \left(\frac{\varepsilon}{\text{keV}} \right)^{1/2} \left(\frac{B}{\text{mG}} \right)^{-3/2} \left(\frac{v_s}{3000 \text{ km s}^{-1}} \right)^{-2} \text{ yr}. \quad (3)$$

Here B , η , and v_s are the strength of the magnetic field, the so-called gyro factor which is defined as the mean free path of the particle divided by its gyroradius, and the shock speed, respectively. Note that the case of $\eta = 1$ is the most efficient acceleration, known as Bohm limit. The characteristic energy of a synchrotron photon (ε) is given by $\varepsilon \approx 0.016(B/\text{mG})(E_e/\text{TeV})^2 \text{ keV}$.

Inoue et al. (2012) showed that the penetration depth of a particle into a dense clump due to its random walk is described with

$$l_{\text{pd}} \simeq (\kappa_d t)^{1/2},$$

$$= 0.1\eta^{1/2} \left(\frac{E}{10 \text{ TeV}} \right)^{1/2} \left(\frac{B}{100 \mu\text{G}} \right)^{-1/2} \left(\frac{t}{10^3 \text{ yr}} \right)^{1/2} \text{ pc}, \quad (4)$$

where t is defined as the time since the high-energy particle started penetrating into the clump. Here, $\kappa_d = 4\eta l_g c/3\pi$ is the diffusion coefficient¹ of a high-energy particle with a gyroradius of l_g .

We confirmed the thermal emission from the shock-core interaction is not dominant for the case of RX J1713.7–3946. The temperature of a proton in a shocked core, which corresponds to the upper limit of the temperature of electrons, is characterized by two parameters: the speed of the transmitted shock in the core and the number density ratio of the diffuse gas and the core. The shock speed in the core is given by $v_{\text{sh,c}} \approx v_{\text{sh,d}} \times (n_d/n_c)^{1/2}$, where $v_{\text{sh,d}}$, n_d , and n_c are the shock speed in the diffuse gas, the number density of the diffuse gas, and the number density of the core, respectively. The ambient density of RX J1713.7–3946 was estimated to be $n_d \sim 0.01 \text{ cm}^{-3}$ from X-ray

¹ If we assume the diffusion in pitch angle is $D_\theta = \pi c/4\eta l_g \sim c/\eta l_g$, the diffusion coefficient becomes $\kappa_d = \eta l_g c/3$.

observations (Slane et al. 1999; Cassam-Chenaï et al. 2004; Takahashi et al. 2008; Tanaka et al. 2008; Katsuda et al. 2015; Tsuji & Uchiyama 2016). High-density objects such as cores and clumps are not heated enough to emit X-rays by the transmitted shock because the shock speed in the core is roughly hundreds of m s^{-1} . The timescale of plasma instability (Kelvin-Helmholtz instability) is of the same order as the so-called “cloud-crushing time”, t_{cc} (Klein et al. 1994). Assuming a cloud with a size of L_c , the cloud-crushing time is given by $t_{\text{cc}} = L_c/v_{\text{sh},c}$. This results in tens of thousands of years, consistently with the estimate in Celli et al. (2019).² Thus, the clump survives against the plasma instability because t_{cc} is much longer than the age of the SNR. Therefore, we presume that the X-ray emitted from the hotspot is attributed to predominantly non-thermal (synchrotron) radiation. A non-thermal origin is also supported by the featureless spectra.

We propose two scenarios for the origin of the hotspot: the X-ray emission originates from “primary electrons and/or from “secondary electrons. In this paper, primary electrons indicates those accelerated by shocks (i.e., the forward shock of the SNR and/or the reflected shock induced by the interaction between the forward shock and the core). Secondary electrons are those produced by the decay of a charged pion, which is one of the products arising from the collision of very-high-energy protons and matters in the core. We note that secondary positrons are also taken into consideration.

In the following subsections, we discuss the two scenarios. Hereafter, we assume that $\eta \approx 1$ and $v_s = 3900 \text{ km/s}$ in the case of RX J1713.7–3946 NW (Uchiyama et al. 2007; Tanaka et al. 2008; Tsuji & Uchiyama 2016; Tsuji et al. 2019).

4.1. Hotspot Originated from Primary Electrons

When the SNR shock is interacting with the dense core, the magnetic field is enhanced, resulting in the strong synchrotron emission from the electrons accelerated at the SNR shock. As shown in Section 3.4, 20 hotspots are variable in the temporal interval of a few years, and 8 hotspots vary even in few months, at more than 3σ confidence levels. The fast time variability of the synchrotron radiation might indicate the presence of amplified magnetic field. Indeed, $B = 0.5\text{--}2.0 \text{ mG}$ could explain the observed year-scale and month-scale variations. Assuming $\varepsilon = 0.5\text{--}10 \text{ keV}$ and $B = 0.5\text{--}2 \text{ mG}$, we obtained $t_{\text{synch}} = 0.2\text{--}6.0 \text{ yr}$ and $t_{\text{acc}} = 0.1\text{--}5.3 \text{ yr}$ from Eq. (2) and Eq. (3), respectively.

Substituting the synchrotron cooling time to Eq. (4), the penetration depth of an electron is written as

$$l_{\text{pd},e} \approx 0.026 \left(\frac{B}{100 \mu\text{G}} \right)^{-3/2} \text{ pc} \quad (5)$$

(Fukui et al. 2012). Note that the penetration depth is independent on the energy of the electrons. It depends on the amplitude of the turbulent magnetic field with the scale of gyroradius of the electrons. Using Eq. (5), $l_{\text{pd},e}$ is roughly estimated to be 2.3 mpc (milli parsec) for $B=0.5 \text{ mG}$, and 0.3 mpc for $B=2.0 \text{ mG}$.

The hotspot seems to be spatially comparable with the size of PSF of *Chandra*, which is approximately 1 arcsec. This corresponds to a radius of $\sim 5 \text{ mpc}$, assuming the distance to the SNR of $\sim 1 \text{ kpc}$ (Fukui et al. 2003). Therefore, the radius of the X-ray bright region in the core is smaller than 5 mpc.

The number density is typically $\sim 10^5\text{--}10^6 \text{ cm}^{-3}$ in the core of molecular clouds. The Atacama Large Millimeter/Submillimeter Array (ALMA) lately found cores with number densities of $\sim 10^7 \text{ cm}^{-3}$ in the regions like Taurus and Orion A (e.g., Onishi et al. 2015; Ohashi et al. 2016, 2018). We therefore assumed $n = 10^5\text{--}10^7 \text{ cm}^{-3}$ for the number density of the core.

The column density (N) is described as

$$N = n \times l_{\text{pd},e} + N_{\text{H,LOS}}, \quad (6)$$

where the first and second terms account for the column density of the core and the line-of-sight column density, respectively. Here, $N_{\text{H,LOS}}$ is assumed to be the column density observed in the central region of the SNR, $0.4 \times 10^{22} \text{ cm}^{-2}$ (Cassam-Chenaï et al. 2004), because the central part is assumed to be less contaminated by the swept-up ISM than the shell region, and thus expected to have the information of the wind-blown cavity. Figure 8 illustrates the relation between the estimated column density (N) and $l_{\text{pd},e}$, assuming n_c of 10^5 , 10^6 , and 10^7 cm^{-3} . In Figure 8, the penetration depth of an electron into magnetic fields of 0.5 mG, 1.0 mG, and 2.0 mG are shown with the solid, dotted, and dashed vertical lines, respectively.

In the case of a strong magnetic field ($B=0.5 \text{ mG}$), $l_{\text{pd},e}$ was calculated to be $\sim 2.3 \text{ mpc}$. This would result in a column density of $N \sim 1 \times 10^{23} \text{ cm}^{-2}$ for $n_c = 10^7 \text{ cm}^{-3}$ (Eq. (6)), which is roughly consistent with the observed values. Note that a lower column density, $N \lesssim 1 \times 10^{22} \text{ cm}^{-2}$, is obtained for $n_c = 10^5\text{--}10^6 \text{ cm}^{-3}$.

In the case of a very strong magnetic field ($B=2 \text{ mG}$), $l_{\text{pd},e}$ becomes $\sim 0.3 \text{ mpc}$, which is much smaller than the size of the core. In this case, the electron cannot deeply penetrate to the core because it would quickly lose its energy in the skin of the core. This reduces the column

² In fact, Celli et al. (2019) used “clump crossing time”, which is calculated as $2L_c/v_{\text{sh},c} \sim 1.4 \times 10^4 \text{ years}$.

density to $N \lesssim 1 \times 10^{22} \text{ cm}^{-2}$ in the case of $n_c = 10^5 - 10^7 \text{ cm}^{-3}$.

The spectral analysis shows that most of the hotspots are characterised by the low N_H and large Γ (Figure 6). This can be interpreted as acceleration in the reflection shock caused by the interaction between the forward shock and the clump. The spectrum of electrons accelerated in the reflection shock becomes steeper due to the low Mach number of the reflection shock (see Inoue et al. (2012) for details).

In summary, for the hotspot originating from primary electrons, the observed properties of the hotspot are interpreted as follows. The rapid flux variation is explained by the amplified magnetic field of 0.5–2 mG. The larger N_H is interpreted as the deeper penetration depth in the $B = 0.5 \text{ mG}$ case, whereas the smaller N_H might be indicative of the shallower penetration depth in a very strong magnetic field of 2 mG. Furthermore, the observed higher Γ might be caused by the reflection shock with the lower Mach number.

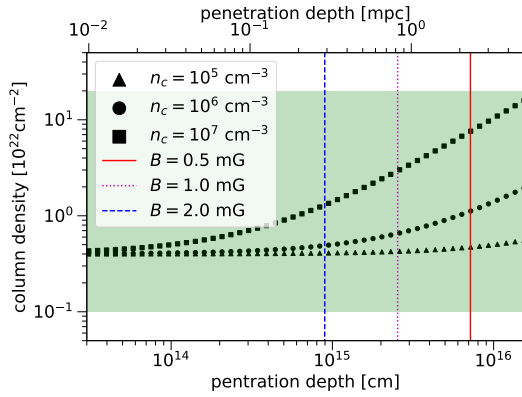


Figure 8. The estimated column density as a function of the penetration depth, assuming the number density of the core of 10^5 , 10^6 , and 10^7 cm^{-3} and using Eq. (6). The vertical red-solid, magenta-dotted, and blue-dashed lines respectively represent the penetration depth of an electron in magnetic fields of 0.5 mG, 1.0 mG, and 2.0 mG using Eq. (5). The observed column density ($N_H = (0.1 - 20) \times 10^{22} \text{ cm}^{-2}$) is shown in the green region.

4.2. Hotspot originated from secondary electrons

The hotspots, the hard hotspot in particular, are likely attributed to the secondary electrons that are produced via the shock-cloud interaction. We assume the same penetration depth of the secondary electrons as that of protons. The hardest hotspot tends to have the largest column density, as shown in Figure 6. The spectrum of high-energy protons in the core is expected to be harder since low-energy protons do not penetrate the clump

deeply, and only very-high-energy protons are capable to reach the core (Gabici & Aharonian 2014; Celli et al. 2019). Therefore, one expects the harder spectrum of the secondary electrons produced via the shock-clump interaction, and also the harder spectrum of the synchrotron radiation from the secondary electrons, which is reconciled with the observed small Γ .

The timescale of proton-proton (pp) interaction is characterized by $t_{pp} \sim 6 \times 10^7 (n/1 \text{ cm}^{-3})^{-1} \text{ yr}$ with the number density of the target matter of n .³ In the case of $n \sim 10^7 \text{ cm}^{-3}$, t_{pp} is ~ 6 years, which is roughly consistent with the observed year-scale variability. Furthermore, the timescale of pp interaction is less than the age of RX J1713.7–3946, given $n = 10^5 - 10^7 \text{ cm}^{-3}$. Substituting the timescale of pp interaction to Eq. (4), we derive the penetration depth of the proton,

$$l_{pd,p} \sim 7.7 \left(\frac{E_p}{10 \text{ TeV}} \right)^{1/2} \left(\frac{B}{100 \mu\text{G}} \right)^{-1/2} \left(\frac{n}{10^7 \text{ cm}^{-3}} \right)^{-1/2} \text{ mpc}, \quad (7)$$

where E_p is the energy of the proton. Note that $l_{pd,p}$ depends on the number density of the core.

In the case of the core with $n = 10^7 \text{ cm}^{-3}$, an energy of about 40 TeV is required for a proton to reach the vicinity of the center of the core, assuming $B = 1 \text{ mG}$ and $l_{pd,p} \sim 5 \text{ mpc}$ in Eq. (7). This results in a column density N of $\sim 10^{23} \text{ cm}^{-2}$, which is roughly consistent with the observed larger N_H . The energy of the proton should be less than 200 TeV, otherwise the proton passes through the core without pp interaction because of the longer penetration depth than the size of the X-ray emitting region (i.e., $l_{pd,p} \geq 10 \text{ mpc}$). Protons with energy of $\sim 40 \text{ TeV}$ ($\leq 200 \text{ TeV}$) can produce the secondary electron responsible for the synchrotron radiation in the X-ray energy band.

In the case of the core with $n = 10^5 \text{ cm}^{-3}$, the proton energy of about 0.4 TeV is required to reach the vicinity of the center of the core, assuming $B = 1 \text{ mG}$ and $l_{pd,p} \sim 5 \text{ mpc}$ in Eq. (7). The energy of the proton should be less than 2 TeV in order to trigger the pp interact within the X-ray emitting region. For protons with energy of $\sim 0.4 \text{ TeV}$ ($\leq 2 \text{ TeV}$), the energy is too low to produce the secondary electron responsible for the synchrotron radiation in the X-ray energy band. Therefore, the very large density of $n = 10^6 - 10^7 \text{ cm}^{-3}$

³ In the derivation of t_{pp} , we used the values of $\sim 40 \text{ mb}$ and 0.45 for the cross section and inelasticity, respectively (Aharonian & Atoyan 1996).

is preferred for the hard hotspot in the scenario of secondary electrons.

In the following, we estimate the synchrotron energy flux emitted from secondary electrons in order to verify the consistency with the observations. The observed flux of the hard hotspot is $\sim 10^{-15}$ – 10^{-14} erg cm $^{-2}$ s $^{-1}$, as derived in Section 3.3.

The energy density of protons in the SNR is described by

$$U_p = \frac{K_p}{V}, \quad (8)$$

$$K_p = \xi E_{\text{SN}} = \xi \times 10^{51} \text{ erg}. \quad (9)$$

Here U_p , K_p , V , ξ , and E_{SN} are the energy density of protons, the total energy of protons filled in the volume of the SNR, the volume of the SNR, the fraction of the kinetic energy transferred from the supernova explosion to protons with energy of 10–1000 TeV, and the typical kinetic energy of supernova explosion, respectively. Suppose that the protons have the power-law distribution of $N(E) \propto E^{-2}$, ξ is derived from the fraction ($\sim 33\%$) of energy occupied by the protons from 10 TeV to 1 PeV in the total energy range from 1 GeV to 1 PeV. This results in $\xi \approx 10\% \times 33\% \approx 0.033$. Note that we assumed the typical fraction of the kinetic energy transferred from the supernova explosion to accelerated protons was 10%. The radius of the remnant is ~ 30 arcmin, which corresponds to ~ 9 pc, assuming $d = 1$ kpc (Fukui et al. 2003). If the cosmic-ray protons are isotropically distributed inside the remnant, the total energy of protons contained in the X-ray emitting region is calculated by

$$W_p = U_p \times \frac{4}{3}\pi R^3, \quad (10)$$

where R is the radius of the X-ray emitting region, namely the core ($R = 5$ mpc). The synchrotron flux emitted by secondary electrons in the characteristic timescale τ is then given by

$$F_X = \frac{\zeta W_p}{4\pi d^2 \tau} \quad (11)$$

$$\sim 8 \times 10^{-20} \left(\frac{\xi}{1} \right) \left(\frac{n}{1 \text{ cm}^{-3}} \right) \text{ erg cm}^{-2} \text{ s}^{-1}. \quad (12)$$

We assume that the fraction of the energy transferred from primary protons to secondary electrons (ζ) is 0.1, and the timescale (τ) is comparable with the timescale of pp interactions, $\tau \sim 6 \times 10^7 (n/1 \text{ cm}^{-3})^{-1}$ yr. We also assume that secondary electrons lose all their energy by synchrotron X-ray radiation in the amplified strong magnetic field.

In the case of $n = 10^6$ – 10^7 cm $^{-3}$ and $\xi = 0.033$, Eq. (12) yields $F_X \sim 10^{-15}$ – 10^{-14} erg cm $^{-2}$ s $^{-1}$,

which reproduces the observed flux level. In the case of $n = 10^5$ cm $^{-3}$, ξ should be ~ 0.33 to reach $\sim 10^{-15}$ erg cm $^{-2}$ s $^{-1}$. $\xi \sim 0.33$, however, is unrealistically large since typical fraction of the kinetic energy transferred from supernova explosion to accelerated protons is ~ 0.1 . We also argued that $n = 10^5$ cm $^{-3}$ is not likely applicable because the expected energy of the proton inside the core is lower for producing the secondary electron responsible for the synchrotron X-ray.

If the hotspots originate from secondary electrons, one expects the hadronic gamma-ray radiation produced from the same protons. It is challenging but very interesting to observe the hadronic gamma-ray radiation from the hotspot and compare it with the X-ray properties. The current gamma-ray telescopes, with the limited angular resolution, make it unrealistic to detect sub-arcsec structures of the hotspots. CTA, however, will provide much better spatial resolution and sensitivity, and allow us to access the gamma-ray information of the hotspots. Neutrino observations may also contribute to this study of revealing the hadronic component.

5. CONCLUSIONS

Using *Chandra* observations of the NW rim of SNR RX J1713.7–3946, we report, for the first time, the detection of a bunch of hotspots likely associated with the SNR. The spectra of the hotspots are well described by an absorbed power-law model with widely distributed parameters of $N_H \sim 10^{21}$ – 10^{23} cm $^{-2}$ and $\Gamma \sim 0.5$ – 6 . These parameters show the larger N_H for the smaller Γ , and are completely different from those in the remnant. We also found that X-ray intensities of about one-third of the 65 hotspots were variable on a yearly scale, and 8 hotspots showed monthly variabilities. We suggest that these hotspots are attributed to the synchrotron X-ray radiation resulting from the interaction between the SNR shock and the dense molecular cores. The synchrotron radiation in the shock-core interaction originates from the accelerated electrons interacting with the core (primary electron origin) and/or electrons produced via accelerated protons colliding with the core (secondary electron origin).

Acknowledgments We thank the anonymous referee for the useful comments. R. H. is supported by Rikkyo University Special Fund for Research. N. T. is supported by the Japan Society for the Promotion of Science (JSPS) KAKENHI grant No. JP17J06025. This work was supported by KAKENHI Grant Numbers 18H03722. Support for this work was provided by the National Aeronautics and Space Administration through Chandra Award Numbers GO9-0074X

and GO1-12092X issued by the Chandra X-ray Observatory Center, which is operated by the Smithsonian Astrophysical Observatory for and on behalf of the National Aeronautics Space Administration under contract NAS8-03060.

Software: CIAO (v4.9)([Fruscione et al. 2006](#)), HEASoft (v6.21)([Nasa High Energy Astrophysics Science Archive Research Center \(Heasarc\) 2014](#)), XSPEC (v12.9.1)([Arnaud 1996](#))

Table 3. The summary of HS01–65

HS ID	Position (α , δ)	Detection significance (σ)	N_H (10^{22} cm $^{-2}$)	Γ	Flux (min) (10^{-14} erg cm $^{-2}$ s $^{-1}$)	Flux (max) (10^{-14} erg cm $^{-2}$ s $^{-1}$)	χ^2/dof	Time variability ($\geq 3\sigma$)
HS01	17:12:04.125	-39:32:10.859	73.4	$4.22^{+0.35}_{-0.30}$	$2.47^{+0.45}_{-0.91}$	$7.19^{+0.98}_{-0.94}$	315.1/289	Y
HS02	17:12:36.796	-39:37:05.230	19.5	$2.95^{+0.22}_{-0.20}$	$4.54^{+0.30}_{-0.60}$	$4.86^{+0.29}_{-0.43}$	76.4/92	N
HS03	17:11:52.997	-39:36:38.134	49.5	$3.84^{+0.53}_{-0.43}$	$1.17^{+0.33}_{-0.47}$	$3.59^{+0.23}_{-0.75}$	155.7/157	N
HS04	17:11:25.658	-39:35:02.662	58.5	$3.37^{+0.26}_{-0.24}$	$4.22^{+0.33}_{-1.01}$	$6.90^{+0.31}_{-1.10}$	188.8/186	YM
HS05	17:11:52.790	-39:38:09.992	26.9	$1.02^{+0.78}_{-0.67}$	$3.62^{+0.24}_{-1.43}$	$23.45^{+0.41}_{-7.85}$	145.2/172	Y
HS06	17:11:57.055	-39:24:07.441	14.1	$5.59^{+1.44}_{-1.03}$	$1.82^{+0.05}_{-0.89}$	$2.30^{+0.21}_{-1.10}$	67.3/79	N
HS07	17:11:52.863	-39:30:51.863	25.7	$2.57^{+0.48}_{-0.42}$	$0.52^{+0.16}_{-0.23}$	$1.83^{+0.31}_{-0.49}$	87.6/109	YM
HS08	17:12:10.965	-39:27:13.396	19.0	$1.91^{+0.28}_{-0.26}$	$0.85^{+0.23}_{-0.29}$	$3.39^{+0.28}_{-0.44}$	77.3/98	YM
HS09	17:11:24.721	-39:31:25.237	25.7	$2.30^{+1.27}_{-0.80}$	≤ 2.82	≤ 6.31	105.2/112	N
HS10	17:11:53.593	-39:27:09.311	17.6	$1.82^{+0.47}_{-0.43}$	$1.00^{+0.24}_{-0.53}$	$2.47^{+0.09}_{-0.78}$	68.6/77	Y
HS11	17:11:18.509	-39:31:23.079	15.6	$4.49^{+1.08}_{-0.84}$	$1.16^{+0.18}_{-0.99}$	$2.51^{+0.15}_{-1.72}$	71.7/96	Y
HS12	17:11:28.422	-39:26:34.798	16.6	$1.32^{+0.84}_{-0.77}$	$2.50^{+0.05}_{-1.48}$	$4.84^{+0.30}_{-2.73}$	46.2/56	N
HS13	17:12:21.943	-39:33:21.784	17.7	$2.17^{+0.45}_{-0.42}$	$0.67^{+0.25}_{-0.25}$	$2.90^{+0.44}_{-0.58}$	42.7/62	Y
HS14	17:11:40.029	-39:31:35.142	15.2	$3.41^{+1.42}_{-0.77}$	$0.38^{+0.15}_{-0.37}$	$1.06^{+0.26}_{-0.85}$	55.4/86	N
HS15	17:11:35.522	-39:26:53.704	15.2	$3.51^{+1.12}_{-0.70}$	$0.57^{+0.08}_{-0.41}$	$1.59^{+0.04}_{-0.88}$	50.8/52	N
HS16	17:12:07.920	-39:33:00.300	13.1	$2.29^{+0.66}_{-0.26}$	$0.43^{+0.29}_{-0.36}$	$2.73^{+0.08}_{-1.48}$	63.6/75	YM
HS17	17:11:53.219	-39:28:57.455	13.6	$1.36^{+0.82}_{-0.70}$	≤ 0.52	$2.92^{+0.46}_{-1.16}$	66.8/82	Y
HS18	17:12:11.875	-39:42:00.805	9.1	$1.39^{+0.42}_{-0.35}$	$0.42^{+0.25}_{-0.39}$	$2.09^{+0.04}_{-1.02}$	16.7/13	N
HS19	17:11:01.348	-39:36:01.349	11.6	$1.29^{+0.75}_{-0.59}$	—	$8.13^{+0.42}_{-1.17}$	43.7/42	YM
HS20	17:11:45.483	-39:28:45.032	14.0	$0.56^{+1.17}_{-0.78}$	$0.94^{+0.54}_{-0.72}$	$2.90^{+0.27}_{-1.14}$	42.4/59	Y
HS21	17:11:24.699	-39:32:00.496	15.6	$1.87^{+0.69}_{-0.56}$	$0.67^{+0.32}_{-0.43}$	$1.60^{+0.29}_{-0.78}$	64.9/69	N
HS22	17:11:55.942	-39:41:24.307	14.0	$2.20^{+0.36}_{-0.32}$	≤ 0.27	$3.93^{+0.41}_{-0.59}$	42.1/50	Y
HS23	17:11:57.698	-39:31:53.047	9.0	$2.31^{+0.72}_{-0.59}$	≤ 0.38	$1.39^{+0.27}_{-0.60}$	87.6/104	Y
HS24	17:11:26.349	-39:40:06.366	11.6	$1.50^{+0.58}_{-0.54}$	$0.72^{+0.11}_{-0.24}$	$1.85^{+0.37}_{-0.63}$	34.2/52	N
HS25	17:12:01.715	-39:34:23.946	11.4	$1.16^{+1.31}_{-1.05}$	≤ 0.54	$3.34^{+0.62}_{-2.71}$	52.5/64	N
HS26	17:11:49.890	-39:43:26.415	7.1	$0.88^{+0.63}_{-0.57}$	≤ 0.47	$4.71^{+0.31}_{-1.23}$	26.8/29	N
HS27	17:11:31.848	-39:31:56.608	9.6	$1.59^{+0.95}_{-0.81}$	≤ 0.35	$1.51^{+0.12}_{-0.92}$	58.7/67	N
HS28	17:11:24.786	-39:32:44.837	10.9	$1.91^{+1.16}_{-0.61}$	≤ 0.20	$1.16^{+0.18}_{-0.70}$	34.0/49	N
HS29	17:11:39.132	-39:44:01.427	6.0	$2.30^{+0.86}_{-0.38}$	$0.74^{+0.03}_{-0.47}$	$0.78^{+0.01}_{-0.52}$	11.0/15	N
HS30	17:12:20.736	-39:36:04.401	9.6	$2.84^{+1.13}_{-0.40}$	≤ 0.19	$1.39^{+0.60}_{-1.28}$	28.6/24	Y
HS31	17:11:48.976	-39:36:12.435	10.0	$13.65^{+10.55}_{-5.85}$	≤ 0.48	≤ 2.93	55.9/70	N
HS32	17:11:46.629	-39:31:06.732	9.3	—	—	—	—	N
HS33	17:12:16.244	-39:29:52.913	6.8	$2.43^{+1.78}_{-1.06}$	≤ 0.35	≤ 1.38	36.0/42	N
HS34	17:12:11.292	-39:30:12.754	6.9	$2.01^{+0.68}_{-0.30}$	≤ 0.12	$1.05^{+0.00}_{-0.47}$	63.2/72	Y
HS35	17:11:41.824	-39:34:31.392	8.8	$2.02^{+0.86}_{-0.56}$	≤ 0.25	$1.55^{+0.05}_{-0.83}$	43.6/50	N

Table 3 continued

Table 3 (continued)

HS ID	Position (α , δ)		Detection significance (σ)	N_H (10^{22} cm^{-2})	Γ	Flux (min) ($10^{-14} \text{ erg cm}^{-2} \text{ s}^{-1}$)	Flux (max) ($10^{-14} \text{ erg cm}^{-2} \text{ s}^{-1}$)	χ^2/dof	Time variability ($\geq 3\sigma$)
HS36	17:11:35.140	-39:34:41.255	11.2	≤ 9.95	$-0.37^{+1.42}_{-1.19}$	$0.30^{+0.25}_{-0.28}$	$3.42^{+0.98}_{-1.79}$	29.0/31	N
HS37	17:12:01.602	-39:41:35.049	7.4	≤ 2.39	$2.66^{+1.25}_{-1.01}$	≤ 0.36	≤ 1.89	19.4/23	N
HS38	17:11:24.442	-39:30:45.768	7.8	$7.51^{+4.17}_{-6.19}$	≥ 3.01	≤ 0.02	≤ 0.73	44.7/53	N
HS39	17:12:05.302	-39:34:03.442	8.0	≤ 1.28	$2.59^{+2.15}_{-0.62}$	≤ 0.12	$0.52^{+0.01}_{-0.51}$	34.7/42	N
HS40	17:11:35.042	-39:33:54.616	9.3	$15.51^{+21.63}_{-14.96}$	$1.23^{+4.41}_{-2.53}$	≤ 0.55	≤ 1.63	31.8/39	N
HS41	17:11:25.888	-39:30:14.223	6.9	$2.90^{+4.80}_{-2.46}$	$4.26^{+3.90}_{-2.22}$	≤ 0.11	≤ 0.74	43.5/49	N
HS42	17:11:31.863	-39:32:05.315	7.4	≤ 1.99	≥ 2.88	≤ 0.06	≤ 0.10	51.2/50	N
HS43	17:11:06.326	-39:29:19.369	7.8	≤ 1.30	$1.10^{+0.84}_{-0.31}$	$0.97^{+0.04}_{-0.46}$	$1.34^{+0.13}_{-0.66}$	10.4/11	N
HS44	17:12:13.337	-39:41:21.576	4.9	≤ 6.98	$1.28^{+4.62}_{-0.79}$	—	≤ 1.10	2.8/2	N
HS45	17:12:04.689	-39:31:39.247	4.8	≤ 2.22	$0.58^{+2.78}_{-0.80}$	≤ 0.26	$0.99^{+0.48}_{-0.89}$	67.4/66	N
HS46	17:11:56.101	-39:34:54.946	7.8	—	—	—	—	—/—	N
HS47	17:11:56.054	-39:26:54.958	6.7	$2.59^{+3.47}_{-2.48}$	$2.48^{+1.93}_{-1.56}$	≤ 0.29	≤ 0.93	22.6/32	N
HS48	17:11:25.488	-39:41:05.711	5.6	$8.15^{+16.92}_{-7.02}$	$-0.01^{+2.21}_{-1.75}$	$0.60^{+0.05}_{-0.58}$	$1.98^{+0.20}_{-1.91}$	32.3/29	N
HS49	17:11:17.037	-39:36:41.864	7.9	≤ 4.56	$3.07^{+1.79}_{-1.35}$	≤ 0.35	≤ 1.72	10.8/24	NM
HS50	17:12:31.583	-39:32:12.191	4.3	—	—	—	—	—/—	N
HS51	17:12:26.721	-39:33:00.127	5.9	≤ 0.47	$3.04^{+1.00}_{-0.34}$	≤ 0.33	≤ 0.71	13.3/20	N
HS52	17:11:27.062	-39:39:06.295	7.2	$11.99^{+16.59}_{-8.40}$	$2.70^{+3.66}_{-1.91}$	≤ 0.40	≤ 2.27	16.0/20	N
HS53	17:11:58.633	-39:29:54.987	5.2	$10.84^{+28.82}_{-8.51}$	≥ 0.16	≤ 0.45	≤ 8.29	38.3/49	N
HS54	17:12:05.491	-39:33:50.944	6.7	≤ 0.16	$1.86^{+0.59}_{-0.42}$	$0.37^{+0.11}_{-0.27}$	$0.79^{+0.18}_{-0.49}$	44.5/58	N
HS55	17:11:38.575	-39:32:20.384	5.7	—	—	—	—	—/—	YM
HS56	17:12:08.933	-39:34:54.495	7.3	—	—	—	—	—/—	N
HS57	17:11:37.148	-39:30:09.914	7.4	≤ 29.63	≥ -2.98	≤ 0.00	≤ 6.06	29.4/33	N
HS58	17:11:49.802	-39:34:44.236	9.0	—	—	—	—	—/—	N
HS59	17:11:59.065	-39:37:38.978	5.8	≤ 0.47	$1.60^{+0.75}_{-0.54}$	≤ 0.16	$0.50^{+0.04}_{-0.32}$	16.6/22	N
HS60	17:10:58.832	-39:31:40.962	6.6	—	—	—	—	—/—	N
HS61	17:11:29.741	-39:27:47.529	6.6	$3.14^{+2.86}_{-2.44}$	$4.77^{+4.44}_{-2.32}$	≤ 0.02	≤ 0.39	20.5/22	N
HS62	17:12:07.730	-39:30:25.835	5.5	≤ 16.01	≥ 4.47	≤ 0.22	≤ 1.15	39.7/46	N
HS63	17:12:12.049	-39:34:45.676	7.5	≤ 0.62	$2.40^{+1.81}_{-0.77}$	—	≤ 0.37	9.8/9	N
HS64	17:11:40.961	-39:35:19.848	6.3	$10.29^{+10.36}_{-7.68}$	≥ 2.19	—	≤ 0.23	12.3/15	YM
HS65	17:11:01.986	-39:34:02.649	6.5	≤ 3.21	$3.27^{+3.45}_{-1.53}$	—	≤ 0.32	7.2/5	N

NOTE— In the columns of column density (N_H), photon index (Γ) and energy flux (min and max), the errors and upper/lower limits indicate 1σ confidence. In the column of time variability, Y and M represent detection of time variation with more than 3σ on a year scale and a month scale, respectively, and N indicates non detection.

REFERENCES

- Abdo, A. A., Ackermann, M., Ajello, M., et al. 2011, *ApJ*, 734, 28, doi: [10.1088/0004-637X/734/1/28](https://doi.org/10.1088/0004-637X/734/1/28)
- Acero, F., Katsuda, S., Ballet, J., & Petre, R. 2017a, *A&A*, 597, A106, doi: [10.1051/0004-6361/201629618](https://doi.org/10.1051/0004-6361/201629618)
- Acero, F., Aloisio, R., Amans, J., et al. 2017b, *ApJ*, 840, 74, doi: [10.3847/1538-4357/aa6d67](https://doi.org/10.3847/1538-4357/aa6d67)
- Ackermann, M., Ajello, M., Allafort, A., et al. 2013, *Science*, 339, 807, doi: [10.1126/science.1231160](https://doi.org/10.1126/science.1231160)
- Aharonian, F., Akhperjanian, A. G., Bazer-Bachi, A. R., et al. 2006, *A&A*, 449, 223, doi: [10.1051/0004-6361:20054279](https://doi.org/10.1051/0004-6361:20054279)
- . 2007, *A&A*, 464, 235, doi: [10.1051/0004-6361:20066381](https://doi.org/10.1051/0004-6361:20066381)
- Aharonian, F. A., & Atoyan, A. M. 1996, *A&A*, 309, 917
- Ambrogio, L., Celli, S., & Aharonian, F. 2018, *Astroparticle Physics*, 100, 69, doi: [10.1016/j.astropartphys.2018.03.001](https://doi.org/10.1016/j.astropartphys.2018.03.001)
- Arnaud, K. A. 1996, *Astronomical Society of the Pacific Conference Series*, Vol. 101, *XSPEC: The First Ten Years*, ed. G. H. Jacoby & J. Barnes, 17
- Axford, W. I., Leer, E., & Skadron, G. 1977, in *International Cosmic Ray Conference*, Vol. 11, *International Cosmic Ray Conference*, 132
- Bell, A. R. 1978, *MNRAS*, 182, 147, doi: [10.1093/mnras/182.2.147](https://doi.org/10.1093/mnras/182.2.147)
- Blandford, R. D., & Ostriker, J. P. 1978, *ApJL*, 221, L29, doi: [10.1086/182658](https://doi.org/10.1086/182658)
- Cassam-Chenaï, G., Decourchelle, A., Ballet, J., et al. 2004, *A&A*, 427, 199, doi: [10.1051/0004-6361:20041154](https://doi.org/10.1051/0004-6361:20041154)
- Celli, S., Morlino, G., Gabici, S., & Aharonian, F. A. 2019, *MNRAS*, 487, 3199, doi: [10.1093/mnras/stz1425](https://doi.org/10.1093/mnras/stz1425)
- Ellison, D. C., Patnaude, D. J., Slane, P., & Raymond, J. 2010, *ApJ*, 712, 287, doi: [10.1088/0004-637X/712/1/287](https://doi.org/10.1088/0004-637X/712/1/287)
- Fesen, R. A., Kremer, R., Patnaude, D., & Milisavljevic, D. 2012, *AJ*, 143, 27, doi: [10.1088/0004-6256/143/2/27](https://doi.org/10.1088/0004-6256/143/2/27)
- Freeman, P. E., Kashyap, V., Rosner, R., & Lamb, D. Q. 2002, *ApJS*, 138, 185, doi: [10.1086/324017](https://doi.org/10.1086/324017)
- Fruscione, A., McDowell, J. C., Allen, G. E., et al. 2006, *Society of Photo-Optical Instrumentation Engineers (SPIE) Conference Series*, Vol. 6270, *CIAO: Chandra's data analysis system*, 62701V
- Fukui, Y., Moriguchi, Y., Tamura, K., et al. 2003, *PASJ*, 55, L61, doi: [10.1093/pasj/55.5.L61](https://doi.org/10.1093/pasj/55.5.L61)
- Fukui, Y., Sano, H., Sato, J., et al. 2012, *ApJ*, 746, 82, doi: [10.1088/0004-637X/746/1/82](https://doi.org/10.1088/0004-637X/746/1/82)
- Funk, S. 2015, *Annual Review of Nuclear and Particle Science*, 65, 245, doi: [10.1146/annurev-nucl-102014-022036](https://doi.org/10.1146/annurev-nucl-102014-022036)
- Gabici, S., & Aharonian, F. A. 2014, *MNRAS*, 445, L70, doi: [10.1093/mnras/slu132](https://doi.org/10.1093/mnras/slu132)
- H.E.S.S. Collaboration, Abdalla, H., Abramowski, A., et al. 2018, *A&A*, 612, A6, doi: [10.1051/0004-6361/201629790](https://doi.org/10.1051/0004-6361/201629790)
- Hiraga, J. S., Uchiyama, Y., Takahashi, T., & Aharonian, F. A. 2005, *A&A*, 431, 953, doi: [10.1051/0004-6361:20047015](https://doi.org/10.1051/0004-6361:20047015)
- Huang, Y., Li, Z., Wang, W., & Zhao, X. 2018, *arXiv e-prints*. <https://arxiv.org/abs/1807.11239>
- Inoue, T., Yamazaki, R., Inutsuka, S.-i., & Fukui, Y. 2012, *ApJ*, 744, 71, doi: [10.1088/0004-637X/744/1/71](https://doi.org/10.1088/0004-637X/744/1/71)
- Jogler, T., & Funk, S. 2016, *ApJ*, 816, 100, doi: [10.3847/0004-637X/816/2/100](https://doi.org/10.3847/0004-637X/816/2/100)
- Katsuda, S., Acero, F., Tominaga, N., et al. 2015, *ApJ*, 814, 29, doi: [10.1088/0004-637X/814/1/29](https://doi.org/10.1088/0004-637X/814/1/29)
- Klein, R. I., McKee, C. F., & Colella, P. 1994, *ApJ*, 420, 213, doi: [10.1086/173554](https://doi.org/10.1086/173554)
- Koyama, K., Kinugasa, K., Matsuzaki, K., et al. 1997, *PASJ*, 49, L7, doi: [10.1093/pasj/49.3.L7](https://doi.org/10.1093/pasj/49.3.L7)
- Koyama, K., Petre, R., Gotthelf, E. V., et al. 1995, *Nature*, 378, 255, doi: [10.1038/378255a0](https://doi.org/10.1038/378255a0)
- Krymskii, G. F. 1977, *Akademiia Nauk SSSR Doklady*, 234, 1306
- Lazendic, J. S., Slane, P. O., Gaensler, B. M., et al. 2004, *ApJ*, 602, 271, doi: [10.1086/380956](https://doi.org/10.1086/380956)
- Moriguchi, Y., Tamura, K., Tawara, Y., et al. 2005, *ApJ*, 631, 947, doi: [10.1086/432653](https://doi.org/10.1086/432653)
- Nasa High Energy Astrophysics Science Archive Research Center (Heasarc). 2014, *HEASoft: Unified Release of FTOOLS and XANADU*. <http://ascl.net/1408.004>
- Ohashi, S., Sanhueza, P., Chen, H.-R. V., et al. 2016, *ApJ*, 833, 209, doi: [10.3847/1538-4357/833/2/209](https://doi.org/10.3847/1538-4357/833/2/209)
- Ohashi, S., Sanhueza, P., Sakai, N., et al. 2018, *ApJ*, 856, 147, doi: [10.3847/1538-4357/aab3d0](https://doi.org/10.3847/1538-4357/aab3d0)
- Okuno, T., Tanaka, T., Uchida, H., Matsumura, H., & Tsuru, T. G. 2018, *PASJ*, 70, 77, doi: [10.1093/pasj/psy072](https://doi.org/10.1093/pasj/psy072)
- Onishi, T., Tokuda, K., Saigo, K., et al. 2015, in *Astronomical Society of the Pacific Conference Series*, Vol. 499, *Revolution in Astronomy with ALMA: The Third Year*, ed. D. Iono, K. Tatematsu, A. Wootten, & L. Testi, 211
- Pfeffermann, E., & Aschenbach, B. 1996, in *Roentgenstrahlung from the Universe*, ed. H. U. Zimmermann, J. Trümper, & H. Yorke, 267–268
- Sano, H., Sato, J., Horachi, H., et al. 2010, *ApJ*, 724, 59, doi: [10.1088/0004-637X/724/1/59](https://doi.org/10.1088/0004-637X/724/1/59)
- Sano, H., Tanaka, T., Torii, K., et al. 2013, *ApJ*, 778, 59, doi: [10.1088/0004-637X/778/1/59](https://doi.org/10.1088/0004-637X/778/1/59)
- Sano, H., Fukuda, T., Yoshiike, S., et al. 2015, *ApJ*, 799, 175, doi: [10.1088/0004-637X/799/2/175](https://doi.org/10.1088/0004-637X/799/2/175)

- Slane, P., Gaensler, B. M., Dame, T. M., et al. 1999, *ApJ*, 525, 357, doi: [10.1086/307893](https://doi.org/10.1086/307893)
- Takahashi, T., Tanaka, T., Uchiyama, Y., et al. 2008, *PASJ*, 60, S131, doi: [10.1093/pasj/60.sp1.S131](https://doi.org/10.1093/pasj/60.sp1.S131)
- Tanaka, T., Uchiyama, Y., Aharonian, F. A., et al. 2008, *ApJ*, 685, 988, doi: [10.1086/591020](https://doi.org/10.1086/591020)
- Tsuji, N., & Uchiyama, Y. 2016, *PASJ*, 68, 108, doi: [10.1093/pasj/psw102](https://doi.org/10.1093/pasj/psw102)
- Tsuji, N., Uchiyama, Y., Aharonian, F., et al. 2019, *ApJ*, 877, 96, doi: [10.3847/1538-4357/ab1b29](https://doi.org/10.3847/1538-4357/ab1b29)
- Uchiyama, Y., Aharonian, F. A., & Takahashi, T. 2003, *A&A*, 400, 567, doi: [10.1051/0004-6361:20021824](https://doi.org/10.1051/0004-6361:20021824)
- Uchiyama, Y., Aharonian, F. A., Tanaka, T., Takahashi, T., & Maeda, Y. 2007, *Nature*, 449, 576, doi: [10.1038/nature06210](https://doi.org/10.1038/nature06210)
- Wang, Z. R., Qu, Q.-Y., & Chen, Y. 1997, *A&A*, 318, L59
- Wilms, J., Allen, A., & McCray, R. 2000, *ApJ*, 542, 914, doi: [10.1086/317016](https://doi.org/10.1086/317016)
- Zirakashvili, V. N., & Aharonian, F. A. 2010, *ApJ*, 708, 965, doi: [10.1088/0004-637X/708/2/965](https://doi.org/10.1088/0004-637X/708/2/965)